



HAL
open science

The oxidation state of titanium in silicate melts

Andrew J. Berry, Patricia M. Doyle, Paul F. Schofield, Laura A. Miller,
Charles Le Losq, Antony D. Burnham, J. Fred W. Mosselmans

► **To cite this version:**

Andrew J. Berry, Patricia M. Doyle, Paul F. Schofield, Laura A. Miller, Charles Le Losq, et al.. The oxidation state of titanium in silicate melts. *Geochimica et Cosmochimica Acta*, 2024, 366, pp.210-220. 10.1016/j.gca.2023.11.014 . insu-04462203

HAL Id: insu-04462203

<https://insu.hal.science/insu-04462203>

Submitted on 16 Feb 2024

HAL is a multi-disciplinary open access archive for the deposit and dissemination of scientific research documents, whether they are published or not. The documents may come from teaching and research institutions in France or abroad, or from public or private research centers.

L'archive ouverte pluridisciplinaire **HAL**, est destinée au dépôt et à la diffusion de documents scientifiques de niveau recherche, publiés ou non, émanant des établissements d'enseignement et de recherche français ou étrangers, des laboratoires publics ou privés.



The oxidation state of titanium in silicate melts

Andrew J. Berry^{a,b,*}, Patricia M. Doyle^{b,c,1}, Paul F. Schofield^b, Laura A. Miller^a, Charles Le Losq^d, Antony D. Burnham^a, J. Fred W. Mosselmans^e

^a Research School of Earth Sciences, Australian National University, Canberra, ACT 2601, Australia

^b Department of Earth Sciences, Natural History Museum, London SW7 5BD, United Kingdom

^c Department of Earth Science and Engineering, Imperial College London, London SW7 2AZ, United Kingdom

^d Institut de Physique du Globe de Paris, Université de Paris Cité, Paris F-75005, France

^e Diamond Light Source, Harwell Science and Innovation Campus, Didcot OX11 0DE, United Kingdom

ARTICLE INFO

Associate editor: Georges Calas

Keywords:

Oxygen fugacity

Oxidation state

Titanium

Silicate glass

XANES spectroscopy

Mare basalt

Calcium aluminium inclusion

Chondrule

ABSTRACT

Titanium occurs as Ti^{3+} , in addition to the more usual Ti^{4+} , in extraterrestrial materials such as Lunar basalts and chondritic meteorites. The proportion of Ti as Ti^{3+} was investigated by Ti K-edge X-ray absorption near edge structure (XANES) spectroscopy for five silicate glass compositions quenched from melts equilibrated at 1400 °C, atmospheric pressure, and oxygen fugacities (fO_2) in log units relative to the fayalite-magnetite-quartz (FMQ) buffer from FMQ+3.3 to FMQ-10.2 (+6.6 to -6.9 log units relative to the iron-wüstite, IW, buffer). All spectra could be well fit using a linear combination of the spectra recorded from the most oxidised and reduced samples of the same composition, indicating that the samples only contain two Ti species. $Ti^{3+}/\Sigma Ti$ (where $\Sigma Ti = Ti^{3+} + Ti^{4+}$) = 0 for the most oxidised samples but is unknown for the most reduced. Thus, the linear combination fit results were used in a regression model in which $Ti^{3+}/\Sigma Ti$ of the reduced end-member was varied to give $Ti^{3+}/\Sigma Ti$ values of the other samples that best fit the thermodynamically expected dependence of $Ti^{3+}/\Sigma Ti$ on fO_2 . The most reduced samples were found to have $Ti^{3+}/\Sigma Ti \sim 0.6$. The resulting modified equilibrium constants of the Ti oxidation reaction, $\log K'$, are linearly correlated with the optical basicity (Λ) parameterisation of melt composition, such that as Λ increases, $Ti^{3+}/\Sigma Ti$ decreases, at constant fO_2 . This correlation allows $Ti^{3+}/\Sigma Ti$ to be predicted for other compositions and, assuming that the temperature dependence of Ti^{3+}/Ti^{4+} is parallel to FMQ, a general equation relating Ti^{3+}/Ti^{4+} to fO_2 was obtained: $\log(Ti^{3+}/Ti^{4+}) = -0.25\Delta FMQ - 0.32(19) - 3.44(32)\Lambda$. This equation was used to predict $Ti^{3+}/\Sigma Ti$ as a function of fO_2 for high-Ti Mare basalt, chondrule (CV and CM), and calcium aluminium inclusion (CAI; Type A and B) compositions. For melts of these compositions $Ti^{3+} = Ti^{4+}$ at $\sim FMQ-10.8$, -9.5, -9.3, -10.6, and -10.2 ($\sim IW-7.5$, -6.2, -6.0, -7.3, and -6.9), respectively, independent of temperature.

1. Introduction

Titanium occurs exclusively as Ti^{4+} in most natural terrestrial materials, however, under reduced conditions it may also occur as Ti^{3+} . For example, Ti^{3+} is found in armalcolite ($(Fe,Mg)Ti_2O_5$) in high-Ti Lunar basalts (Anderson et al., 1970; Friel et al., 1977) and in both hibonite ($Ca(Al,Ti)_{12}O_{19}$; Beckett et al., 1988; Doyle et al., 2014; Berry et al., 2017) and fassaite ($Ca(Mg,Ti,Al)(Al,Si)_2O_6$; Dowty and Clark, 1973; Simon et al., 2007) in calcium aluminium inclusions (CAI) in chondritic meteorites.

The redox variability of Ti means that it may record the oxygen

fugacity (partial pressure of oxygen; fO_2) of extraterrestrial processes under conditions where the common terrestrial fO_2 sensor, the oxidation state of Fe (Fe^{3+}/Fe^{2+} ; e.g. O'Neill et al., 2018), cannot be used because of the presence of Fe metal and absence of Fe^{3+} . The fO_2 at which $Ti^{3+} = Ti^{4+}$ has been estimated to be IW-7, where IW is the iron-wüstite ($Fe-FeO$) buffer (Papike et al., 2005). Other common elements that are redox variable under reduced conditions include V ($V^{2+} = V^{3+}$ at IW-4) and Cr ($Cr^{2+} = Cr^{3+}$ at IW) (Berry and O'Neill, 2004; Papike et al., 2005; Sutton et al., 1993, 2005).

Ti^{3+} has been identified traditionally by optical absorption spectroscopy (Burns and Huggins, 1973), electron paramagnetic resonance

* Corresponding author.

E-mail address: Andrew.Berry@anu.edu.au (A.J. Berry).

¹ Present address: Department of Geological Sciences, University of Cape Town, Rondebosch 7701, South Africa.

(EPR; also called electron spin resonance or ESR) spectroscopy (Schreiber et al., 1978; Beckett et al., 1988), and redox titrations (Johnston, 1965; Schreiber et al., 1978; Tranell et al., 2002). For silicate melts Ti^{3+}/Ti^{4+} has been determined by redox titrations for $Na_2O \cdot 2SiO_2$ at 1085 °C and four values of fO_2 and at four temperatures between 1000 and 1300 °C and one fO_2 (Johnston, 1965), forsterite-anorthite-silica (FAS) and forsterite-anorthite-diopside (FAD) compositions at 1500 and 1550 °C and six fO_2 s (Schreiber et al., 1978), albite-diopside-anorthite (ADA2) at 1250 °C and one fO_2 (Schreiber et al., 1982), and a set of CaO-rich synthetic slag compositions at 1500 °C and one fO_2 (Morizane et al., 1999). In addition, Ti^{3+}/Ti^{4+} was estimated from the solubility of rutile in an anorthite-diopside eutectic composition, to which was added 32 wt% TiO_2 , at 1300 °C and seven fO_2 s spanning < 1.3 log units (Borisov et al. 2004). When Ti^{3+}/Ti^{4+} was determined over a range of fO_2 s, even though the proportion of Ti as Ti^{3+} in most cases was only between 0 and 7 %, the relationship between Ti^{3+}/Ti^{4+} and fO_2 could be described by the expected expression:

$$\log \frac{Ti^{3+}}{Ti^{4+}} = -\frac{1}{4} \log fO_2 - \log K' \quad (1)$$

where $\log K'$ is a modified equilibrium constant (see Berry and O'Neill, 2004) that is equal to $-1/4E_M^* = -E_M'$ (the notation in Schreiber et al., 1978 and Schreiber, 1987 for the reduction potential of an element M in a silicate melt). Eq. (1) can be rearranged to give:

$$\frac{Ti^{3+}}{\Sigma Ti} = \frac{1}{1 + 10^{(0.25 \log fO_2 + \log K')}} \quad (2)$$

where $\Sigma Ti = Ti^{3+} + Ti^{4+}$. Fits to the literature data using this equation, plotted relative to the fayalite-magnetite-quartz (FMQ) and IW buffers, are shown in Fig. 1 and illustrate the small range of the $Ti^{3+}/\Sigma Ti$ values, the small number of fO_2 values per study, and the scatter in the data. These studies indicate that the fO_2 at which $Ti^{3+} = Ti^{4+}$ depends on composition (cf. FAS and FAD at constant temperature) and, relative to FMQ, increases with increasing temperature for FAS and FAD but is constant with temperature for $Na_2O \cdot 2SiO_2$. The available data has been used to derive a model relating Ti^{4+}/Ti^{3+} to fO_2 , temperature and composition (Borisov, 2012).

X-ray absorption near edge structure (XANES) spectroscopy can be used to determine $M^{n+}/\Sigma M$ of a redox variable element (M) in glasses with an accuracy of 0.02 or better (e.g. Berry et al., 2018; Berry and O'Neill, 2004; Burnham et al., 2015; Burnham and Berry, 2014). XANES has a

number of advantages over redox titrations including shorter times for data acquisition, which facilitates the analysis of large numbers of samples, high spatial resolution (micron to sub-micron), and suitability for Fe-bearing compositions. For Ti^{4+} the energy and intensity of the 1s-3d pre-edge feature can be used to identify the coordination environment (e.g. Farges et al., 1996; Berry et al., 2007). For Ti^{3+} the absorption edge occurs, as expected, at lower energies than for Ti^{4+} (Waychunas, 1987) and Ti K-edge XANES spectroscopy has been used to determine $Ti^{3+}/\Sigma Ti$ in olivine, pyroxene and hibonite (Simon et al., 2007; Doyle et al., 2016; Sutton et al., 2017; Simon and Sutton, 2017). Here we use Ti K-edge XANES spectroscopy to determine $Ti^{3+}/\Sigma Ti$ for five geologically relevant melt compositions with the aim of parameterising the effect of composition on $Ti^{3+}/\Sigma Ti$. EPR spectra were also recorded for one of these compositions.

2. Experimental

Five compositions in the system CaO-MgO- Al_2O_3 - SiO_2 (CMAS) were selected to investigate the effect of melt composition on $Ti^{3+}/\Sigma Ti$. These include the anorthite-diopside eutectic (AD) and four compositions obtained from the eutectic by the addition of either forsterite (AD+Fo), enstatite (AD+En), wollastonite (AD+Wo), or quartz (AD+Qz) in amounts close to their maximum solubility at 1400 °C, to which 1 wt% TiO_2 was added. Similar CMAS compositions have been used previously in studies of $Cr^{2+}/\Sigma Cr$, $Ce^{3+}/\Sigma Ce$, and $Eu^{2+}/\Sigma Eu$ (Berry and O'Neill, 2004; Burnham et al., 2015; Burnham and Berry, 2014). The compositions were prepared by grinding and mixing reagent grade SiO_2 , Al_2O_3 , MgO, TiO_2 (all dried at 1000 °C) and $CaCO_3$ (dried at 300 °C) under acetone using an agate mortar and pestle. The resulting powders were mixed with polyethylene oxide and water to form a paste and mounted on wire loops of either Pt or Re and equilibrated at 1400 °C and atmospheric pressure in a vertical gas mixing furnace using CO_2 -CO to control the fO_2 at log values between -3.1 and -14 (calculated using the thermodynamic data in Chase, 1998), or 3.3 and -7.6 in log units relative to FMQ (O'Neill et al., 2018). Multiple loops (one for each composition) were suspended from a “chandelier”. At $\log fO_2 = -3$ (FMQ+3.3) the loops and chandelier were made of Pt, at $-3 > \log fO_2 \geq -12$ (FMQ-5.6) both Pt and Re loops were used with a Pt chandelier, and at $\log fO_2 \leq -13$ (FMQ-6.6) the loops were Re and the chandelier ceramic. The $\log fO_2$ s of the experiments at -11 to -14 were checked using the Fe content of AD (Ti-free) equilibrated on a loop of Fe simultaneously with the other samples (e.g. Berry et al., 2018). For experiments at $\log fO_2 \leq$

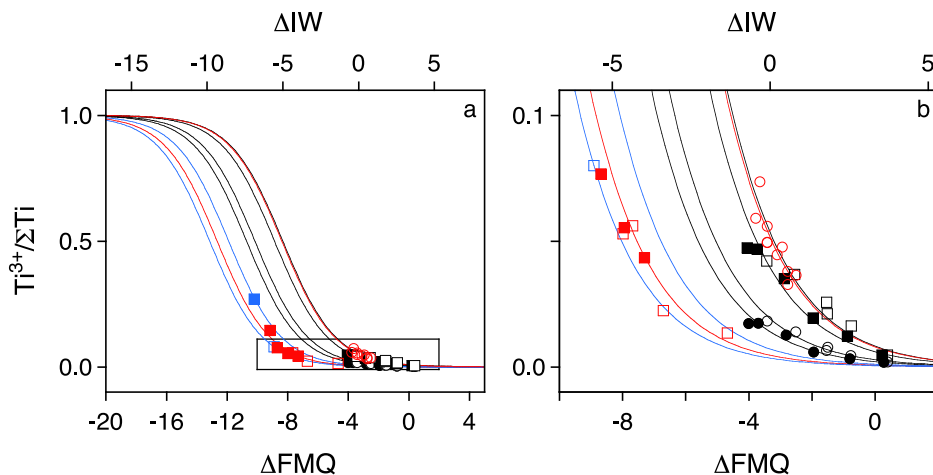


Fig. 1. $Ti^{3+}/\Sigma Ti$ as a function of oxygen fugacity in log units relative to the fayalite-magnetite-quartz (FMQ) and iron-wüstite (IW) buffers for compositions FAD (black circles) and FAS (black squares) at 1550 °C (open) and 1500 °C (closed) from Schreiber et al. (1978), ADA2 at 1250 °C (open blue square; Schreiber et al., 1982), ADTi at 1300 °C (open red circles; Borisov et al. 2004), “slag” at 1500 °C (closed blue square; Morizane et al., 1999), and $Na_2O \cdot 2SiO_2$ at 1085 °C (closed red squares) and a constant fO_2 buffer at 1000, 1085, 1200 and 1300 °C (open red squares; Johnston, 1965). The solid lines, in colours matching the related symbols, correspond to Eq. (2) using the calculated $\log K'$ for each composition. (b) shows the region defined by the inset in (a). IW is offset from FMQ by 3.3 (the difference in values at 1400 °C).

–16.1 (FMQ-9.7) the powders were pressed into pellets, which were loaded into wells drilled in a graphite block (as described in O'Neill and Berry, 2006), and equilibrated with CO, or CO diluted with Ar, to achieve nominal $\log f_{\text{O}_2}$ s as low as –20 (FMQ-13.6; for the equilibrium $\text{CO} = 1/2\text{O}_2 + \text{C}$, $\log f_{\text{O}_2} = 2\log K + 2\log f_{\text{CO}}$, where K is the equilibrium constant and $2\log K = -16.1$ at 1400 °C). After ~20 h the melts were quenched in water. For further details of the experimental technique see Burnham et al., 2015. The resulting glasses (3–5 mm beads) were either mounted in epoxy resin and polished (XANES) or powdered using a mortar and pestle (EPR). Pellets of Ti_2O_3 , TiO_2 , and $\text{Ni}_{2.62}\text{Ti}_{0.69}\text{O}_4$ (spinel) mixed with BN (~1 wt% Ti) and polycrystalline Ti-bearing synthetic forsterite mounted in epoxy resin were prepared previously (Doyle et al., 2016; Berry et al., 2007).

The composition of each glass was determined by electron probe microanalysis (EPMA) using a Cameca SX-100 operating at 20 kV and 20 nA, with LTAP (for Si, Al and Mg), PET (for Ca), LPET (for Ti) and LLIF (for Fe) crystals. Wollastonite (Si and Ca), corundum (Al), forsterite (Mg), rutile (Ti), and fayalite (Fe) were used as standards.

Titanium K-edge XANES spectra were recorded at I18 of Diamond Light Source, UK (Mosselmans et al., 2009). The excitation energy was selected using a Si(111) double crystal monochromator and calibrated by defining the first peak in the derivative spectrum of Ti foil, recorded in transmission mode, to be at 4966.4 eV. The energy resolution at the Ti K-edge was 0.70 eV, which when coupled with the Ti $K\alpha$ core-hole width of 0.94 eV (Krause and Oliver, 1979) resulted in a spectral resolution of 1.2 eV. The beam was focused using Rh coated KB mirrors to $\sim 3 \times 3 \mu\text{m}$, although the penetration depth of Ti K-edge X-rays in the glasses studied (approximated as one absorption length) is $\sim 18 \mu\text{m}$. The KB mirrors were also used to reject high energy harmonics. Fluorescence was recorded using a nine-element Ge detector and the distance between the detector and sample was adjusted to ensure that the total incoming count rate (and hence dead time) was approximately constant for each sample and within the linear range of the signal processing electronics. Samples were mounted at 45° to both the incident beam and the detector. Spectra were recorded from 4950 to 5200 eV with a step size of 1.0 eV for the baseline (4950–4962 eV), 0.1 eV for the pre-edge (4962–4975), 0.2 eV for the absorption edge (4975–5015) and 5.0 eV above the edge, with a count time of 1 s per point, giving a total spectral acquisition time of 15–20 min. The possibility of beam-induced changes in the oxidation state of Ti was investigated by recording 10 replicate spectra of the pre-edge region (0.2 eV steps, 1 s per point, < 2 min per spectrum) from the same spot of samples equilibrated at nominally FMQ-5.6 and FMQ-13.6. The Ti $K\alpha$ fluorescence intensity was dead-time corrected, normalised to the intensity of the incident beam, and the resulting spectra normalised using Athena (Ravel and Newville, 2005).

EPR spectra were recorded using a Bruker EMXmicro spectrometer at the EPSRC EPR Facility (University of Manchester, UK). A second set of AD samples were prepared in the same way, powdered, and loaded to a height of 7 mm in silica glass tubes with a diameter of 4 mm, which were placed in the centre of the resonant cavity of the spectrometer. X-band spectra (9.45 GHz) were recorded at room temperature from 3050 to 3950 G with a modulation amplitude of 5 G. The working power was 20 dB and the time constant and conversion time were 20 and 40 ms, respectively, resulting in spectral acquisition times of ~ 5 min.

3. Results

Melts were equilibrated at 10 f_{O_2} s, nominally spanning 17 log units (FMQ+3.3 to FMQ-13.7). The resulting glasses varied from colourless (FMQ+3.3) to pale pink (FMQ-3.0) to deep purple, with the intensity of the colour increasing with decreasing f_{O_2} . The samples are homogeneous except for the AD+Qz glasses, which contained minor amounts of crystalline SiO_2 . These crystals had a negligible effect on the composition of each glass and contained negligible amounts of Ti. For compositions equilibrated on both Pt and Re loops the Ti contents of the glasses were identical at FMQ-3, but 20 % and 40 % lower for the samples

mounted on Pt at FMQ-4.6 and FMQ-5.6, respectively. This decrease is consistent with Ti alloying with Pt under reduced conditions (e.g. Jurewicz et al., 1995). The results reported here are for the samples prepared using Re loops. The average glass compositions, determined from multiple analyses of the samples prepared at all f_{O_2} s, are given in Table 1. The compositions of the AD glasses on Fe loops, and the $\log f_{\text{O}_2}$ s calculated from the Fe content of each glass, which are all close to the nominal values, are given in Supplementary Table 1.

Ti K-edge XANES spectra of the standard compounds are shown in Doyle et al. (2016) and are consistent with those reported previously (Berry et al., 2007). Spectra for the AD composition are shown in Fig. 2 and for the other four compositions in Supplementary Fig. 1. The spectra exhibit systematic changes in the intensity and shape of the pre-edge feature ~ 4970 eV and in the energy of the absorption edge as a function of f_{O_2} . The replicate spectra of the pre-edge regions are essentially identical and there were no systematic differences that could indicate beam-induced changes in oxidation state. Each of the 10 replicate pre-edge spectra took less than 2 min to acquire with the total beam exposure time being similar to that required to record a single full spectrum. The pre-edge was fit between 4950 and ~ 4980 eV (the energy where the normalised intensity is 0.5) to three pseudo-Voigt peaks, constrained to have the same line-shape, simultaneously with the background, which was modeled as three additional pseudo-Voigt functions, one to simulate the absorption edge, one to account for the edge shoulder at ~ 4977 eV, and one to provide an offset from the baseline that was effectively a sloping line. The pre-edge multiplet could be well fit using only two pseudo-Voigt peaks, however, the addition of a third, low-intensity, component ~ 4967 eV produced a better fit to the low-energy tail. The pre-edge was parameterised using the intensity weighted energy (centroid) of the three peak components. The fits to the spectra of the AD glasses prepared under the most oxidised and reduced conditions are shown in Fig. 3 and the centroid values are given in Supplementary Table 2. The absorption edge was parameterised using the energy at a normalised intensity of 0.8. The value of 0.8 was chosen arbitrarily but corresponds to a part of the edge that is free of structure. This way of defining the edge energy was used in preference to the edge peak in the derivative spectrum because it is simple and had better precision. These edge energies for all glasses are also given in Supplementary Table 2.

The variations of the pre-edge centroid and absorption edge energy with f_{O_2} are shown in Fig. 4. The data were fit to a modified version of Eq. (2) that describes the variation of a feature (rather than $\text{Ti}^{3+}/\Sigma\text{Ti}$) with f_{O_2} (see Burnham et al., 2015). If the feature is linearly related to $\text{Ti}^{3+}/\Sigma\text{Ti}$ then the coefficient of $\log f_{\text{O}_2}$ should be 0.25 (as in Eq. (2)). For the fits shown in Fig. 4 the coefficient was fixed at 0.25, however, values of 0.49(11) and 0.37(5) were obtained (centroid and edge, respectively) if it was allowed to vary. The fits, and hence values of $\log K'$ (3.68(13) and 3.65(8) for the centroid and edge, respectively, with the coefficient fixed at 0.25), are strongly affected by the data at –18 and –20 (FMQ-11.6 and –13.6). The small differences in the spectra of the samples prepared at –16, –18 and –20 (FMQ-9.7, –11.6 and –13.6) could indicate that $\text{Ti}^{3+}/\Sigma\text{Ti}$ is approaching 1 over this range, however, the accuracy of the f_{O_2} values at these extremely reducing conditions is uncertain (see Discussion).

To quantify the overall spectral variation with f_{O_2} , rather than just that of a particular feature, each spectrum was fit, between 4960 and 5000 eV, to a linear combination (LCF) of the spectra of the most oxidised and reduced samples of that composition. The resulting fits are excellent and examples are shown in Fig. 5. The proportions of each end-member determined by the fits are given in Supplementary Spreadsheet 1. Although it is reasonable to assume that $\text{Ti}^{3+}/\Sigma\text{Ti} = 0$ for the most oxidised samples, $\text{Ti}^{3+}/\Sigma\text{Ti}$ of the most reduced samples are unknown and thus $\text{Ti}^{3+}/\Sigma\text{Ti}$ for the intermediate samples cannot be determined directly from the fit results. However, $\log(\text{Ti}^{3+}/\text{Ti}^{4+})$ should have a 0.25 dependence on $\log f_{\text{O}_2}$ (Eq. (1)) and this constraint can be used to determine the $\text{Ti}^{3+}/\Sigma\text{Ti}$ value of each reduced end-member that gives $\text{Ti}^{3+}/\Sigma\text{Ti}$ values of all the intermediate samples that best fit the expected

Table 1

Average glass compositions (wt%) determined by EPMA, the number of analyses (n), optical basicity (Λ) and NBO/T calculated for each composition, and values of $\log K'$ determined from the XANES spectra. Errors are one standard deviation.

Composition	SiO ₂	Al ₂ O ₃	MgO	CaO	TiO ₂	Total	n	Λ	NBO/T	$\log K'$
AD	49.96(49)	15.44(17)	10.59(9)	23.27(30)	1.03(1)	100.29(61)	105	0.6094(10)	0.917(13)	4.001
AD+Fo	49.15(59)	13.19(12)	17.41(19)	19.83(31)	1.04(1)	100.62(70)	111	0.6127(12)	1.204(18)	4.012
AD+Wo	51.49(44)	6.25(8)	4.27(5)	37.43(46)	1.02(2)	100.46(64)	117	0.6345(14)	1.435(20)	4.096
AD+En	54.09(62)	9.53(21)	21.66(41)	14.31(37)	1.06(3)	100.65(86)	134	0.5986(14)	1.271(26)	3.938
AD+Qz	65.86(36)	10.03(27)	6.98(13)	15.30(33)	1.13(2)	99.30(57)	106	0.5633(10)	0.532(12)	3.852

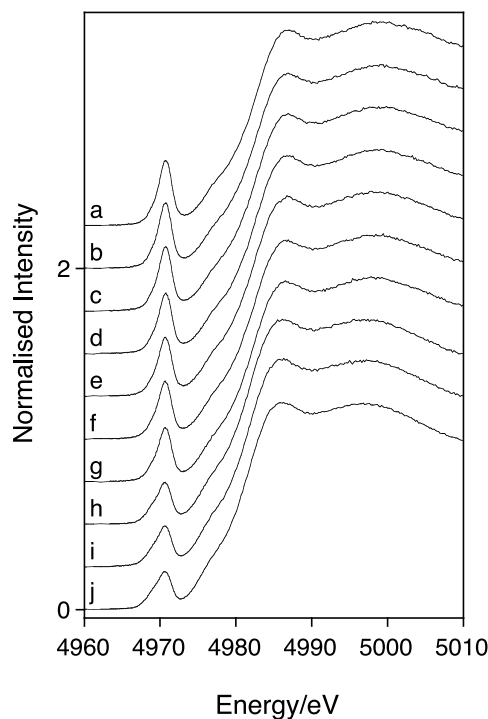


Fig. 2. Normalised Ti K-edge XANES spectra of AD glasses containing 1 wt% TiO₂ quenched from melts equilibrated at 1400 °C and nominal $\log f_{O_2}$ s relative to the fayalite-magnetite-quartz (FMQ) buffer of (a) +3.3, (b) -3.0, (c) -4.6, (d) -5.6, (e) -6.6, (f) -7.1, (g) -7.6, (h) -9.7, (i) -11.6, and (j) -13.6. Spectra are offset for clarity.

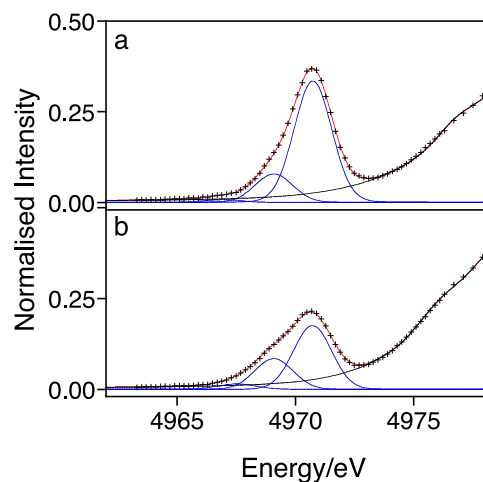


Fig. 3. Pre-edge region of the Ti K-edge XANES spectra of AD glass quenched from melts equilibrated at 1400 °C and nominal $\log f_{O_2}$ s of (a) FMQ+3.3, and (b) FMQ-13.6. The data are denoted by the symbols, and the fit (red), background (black), and pre-edge components (blue) by the solid lines.

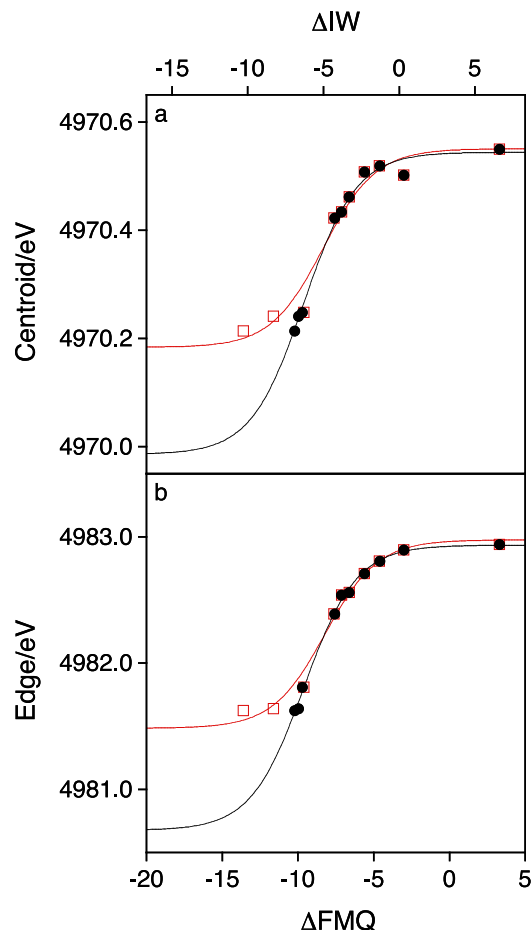


Fig. 4. (a) The energy of the pre-edge centroid, and (b) the energy of the absorption edge at a normalised intensity of 0.8, for the AD composition as a function of f_{O_2} in log units relative to the FMQ and IW buffers. The red squares correspond to the nominal f_{O_2} s and the black circles to those determined by the model. The red and black curves are fits to the data using a modified form of Eq. (2). Uncertainties are smaller than the symbols.

function (Eq. (2)). Further, $\log f_{O_2}$ values can be optimised as part of the fit. Thus, a non-linear least squares regression model was created to determine $Ti^{3+}/\Sigma Ti$ of the most reduced sample, $\log f_{O_2}$, and $\log K'$ by minimising χ^2 , which is defined here as the error weighted difference between the observed and calculated $Ti^{3+}/\Sigma Ti$ and the nominal and calculated $\log f_{O_2}$:

$$\chi^2 = \Sigma \left[\left(\frac{Ti^{3+}}{\Sigma Ti} \right)_{obs} - \left(\frac{Ti^{3+}}{\Sigma Ti} \right)_{cal} \right]^2 / \left[\pm (\text{fit}) \times \left(\frac{Ti^{3+}}{\Sigma Ti} \right)_{-20} \right]^2 + \Sigma \left[\left(\log f_{O_2} \right)_{nom} - \left(\log f_{O_2} \right)_{cal} \right]^2 / \pm (\log f_{O_2})^2 \quad (3)$$

where $(Ti^{3+}/\Sigma Ti)_{obs}$ is determined from the proportions and $Ti^{3+}/\Sigma Ti$ values of the oxidised and reduced $((Ti^{3+}/\Sigma Ti)_{-20})$ components in the LCF, $(Ti^{3+}/\Sigma Ti)_{cal}$ is from Eq. (2), $(\log f_{O_2})_{nom}$ is the nominal $\log f_{O_2}$ of the experiment, and $(\log f_{O_2})_{cal}$ is the $\log f_{O_2}$ determined by the model.

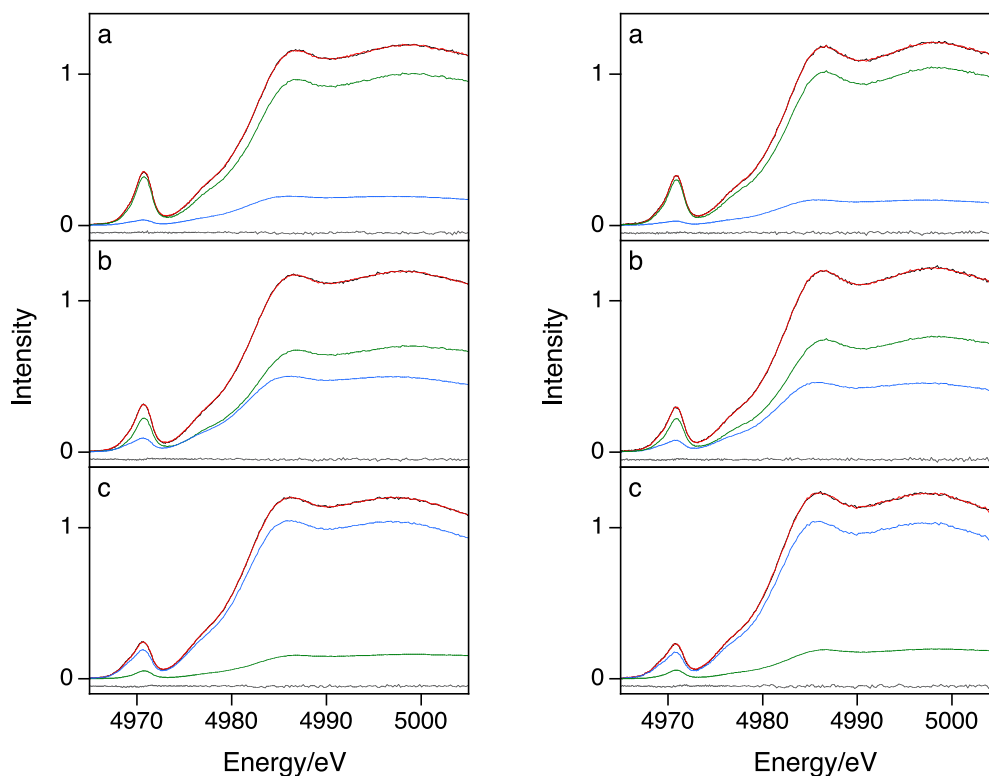


Fig. 5. Ti K-edge XANES spectra (black) of AD (left) and AD+Wo (right) glasses quenched from melts equilibrated at 1400 °C and nominal $\log fO_2$ s of (a) FMQ-5.6, (b) FMQ-7.6, and (c) FMQ-9.7. The spectra were fit (red) using a linear combination of the spectra of the most oxidised (FMQ+3.3, green) and reduced (FMQ-13.6, blue) glasses; the residual is shown in grey.

The uncertainty in the LCF, \pm (fit), was estimated to be 0.015 and the uncertainty in $\log fO_2$, \pm ($\log fO_2$), was assumed to be 0.1 at -3.1 and 0.03 at all other values (see Jayasuriya et al., 2004), except for -18 and -20 where uncertainties of 1 and 2, respectively, were considered reasonable. All five compositions were equilibrated at each fO_2 values. Thus, the data for all compositions were minimised in a single model. The reduced χ^2 of the resulting fit was 1.1 indicating that the data, within the estimated uncertainties, are very well described by the model. The calculated $Ti^{3+}/\Sigma Ti$ and $\log fO_2$ values of each sample are given in Table 2, and the values of $\log K'$ for each composition are given in Table 1. The resulting relationships between $Ti^{3+}/\Sigma Ti$ and ΔFMQ are shown in Fig. 6, together with the sigmoidal curve defined by the corresponding $\log K'$. A spreadsheet containing the model is provided as Supplementary Spreadsheet 1.

It is now possible to calculate the Ti^{3+} (and Ti^{4+}) end-member spectra that best fit the intermediate spectra in the proportions

defined by the calculated $Ti^{3+}/\Sigma Ti$ values. For each composition, a matrix with the recorded XANES spectra, y_{ij} , and a matrix with the fractions of Ti^{3+} and Ti^{4+} , C_{ik} , were defined. Assuming a linear problem, $C_{ik} S_{kj} = y_{ij}$, where S_{kj} is a matrix with the Ti^{3+} and Ti^{4+} end-member spectra, S_{kj} was obtained by solving

$$S_{k,j} = (C_{i,k}^T C_{i,k})^{-1} C_{i,k}^T y_{i,j}, \quad (4)$$

where T is the transpose operator, using Python and the NumPy library (Harris et al., 2020). The calculated Ti^{3+} end-member spectra are shown in Fig. 7a for AD, AD + Wo and AD + Qz (the spectra of AD + En and AD + Fo are similar to that of AD and were omitted for clarity). The pre-edge region of the AD spectrum is shown in Supplementary Fig. 2. To our knowledge, this is the first time that the K-edge XANES spectrum of Ti^{3+} in a silicate glass has been determined. The calculated spectra of Ti^{4+} in the same compositions are shown in Fig. 7b and are essentially indistinguishable from those recorded from the most oxidised samples. For

Table 2

$Ti^{3+}/\Sigma Ti$ values calculated for glasses quenched from melts equilibrated at 1400 °C and the nominal (nom) and calculated (cal) fO_2 s in log units relative to both the conventional standard state and fayalite-magnetite-quartz buffer (ΔFMQ); $\log fO_2$ relative to the iron-wüstite buffer (ΔIW) = $\log fO_2$ calc. + 9.71. The uncertainty in $Ti^{3+}/\Sigma Ti$ is estimated to be similar to that of the LCF (0.015).

$\log fO_2$ nom	$\log fO_2$ cal	ΔFMQ cal	$Ti^{3+}/\Sigma Ti$				
			AD	AD+Fo	AD+Wo	AD+En	AD+Qz
-3.1	-3.10	3.29	0.000	0.000	0.000	0.000	0.000
-9.4	-9.40	-3.01	0.019	0.023	0.020	0.032	0.014
-11.0	-10.99	-4.60	0.042	0.042	0.040	0.058	0.069
-12.0	-12.01	-5.62	0.094	0.087	0.073	0.109	0.129
-13.0	-13.01	-6.62	0.156	0.150	0.125	-	-
-13.5	-13.52	-7.13	0.185	0.190	0.165	0.226	0.262
-14.0	-13.98	-7.59	0.243	0.239	0.198	0.248	0.293
-16.1	-16.10	-9.71	0.511	0.500	0.451	0.558	0.622
-18.0	-16.35	-9.96	0.551	0.551	0.498	0.592	0.605
-20.0	-16.62	-10.23	0.591	0.579	0.539	0.613	0.674

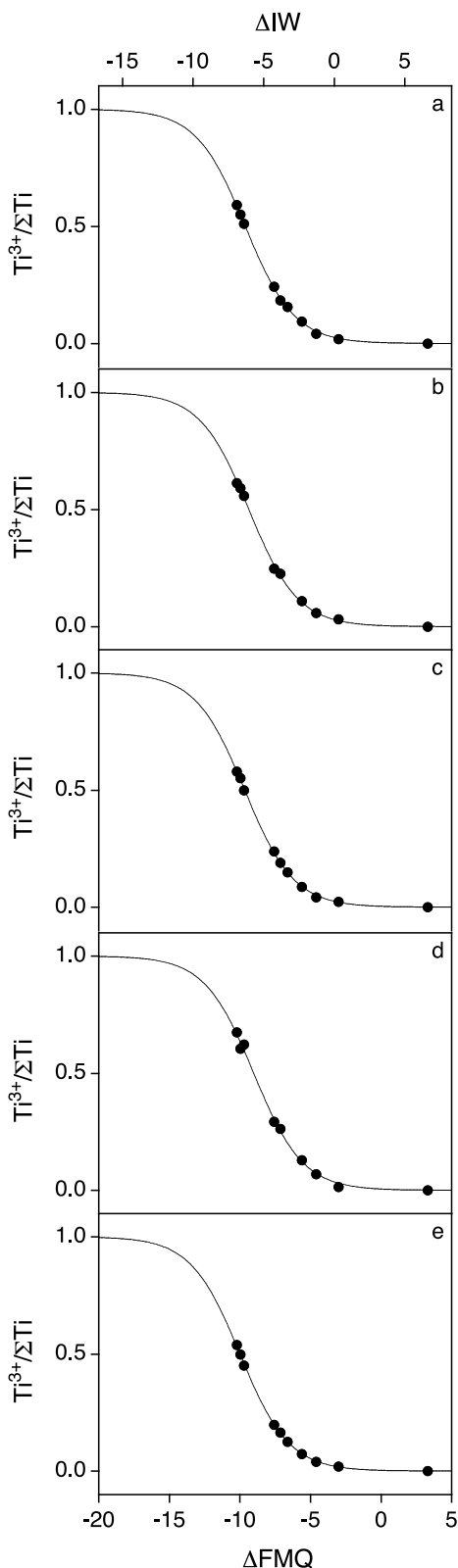


Fig. 6. $\text{Ti}^{3+}/\Sigma\text{Ti}$ as a function of $f\text{O}_2$ in log units relative to FMQ and IW for the (a) AD, (b) AD+En, (c) AD+Fo, (d) AD+Qz, and (e) AD+Wo compositions. The symbols correspond to the $\text{Ti}^{3+}/\Sigma\text{Ti}$ and $\log f\text{O}_2$ values determined for each sample from the model and the curves to Eq. (2) using the calculated $\log K^*$.

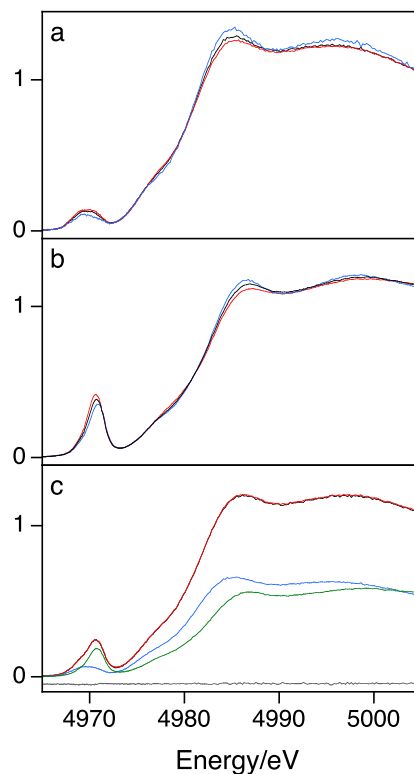


Fig. 7. Calculated Ti K-edge XANES spectra of (a) glasses with $\text{Ti}^{3+}/\Sigma\text{Ti} = 1$, and (b) $\text{Ti}^{3+}/\Sigma\text{Ti} = 0$ for AD (black), AD+Wo (blue) and AD+Qz (red). (c) Ti K-edge XANES spectrum recorded from AD equilibrated at 1400 °C and FMQ-9.7 (black) and the spectrum obtained by summing the calculated AD spectra with $\text{Ti}^{3+}/\Sigma\text{Ti} = 1$ (blue) and 0 (green) in the proportions determined by the model (i.e. $\text{Ti}^{3+}/\Sigma\text{Ti} = 0.511$; red); the difference between the experimental and simulated spectra is shown in grey.

both the Ti^{3+} and Ti^{4+} spectra there are small differences with composition that are likely to be due to small differences in the coordination environment (e.g. Farges et al., 1996). The energy and intensity of the Ti^{4+} pre-edge feature suggests predominantly five-fold coordination (Farges et al., 1996), which is consistent with previous determinations of Ti^{4+} coordination in basaltic glasses (Farges and Brown, 1997). It is not possible to infer the coordination environment of Ti^{3+} due to the small number of compounds (all with Ti^{3+} in six-fold coordination) for which spectra have been reported (e.g. Waychunas, 1987; Doyle et al., 2016). The simulated spectra obtained by summing the Ti^{3+} and Ti^{4+} end-member spectra in the proportions defined by the calculated $\text{Ti}^{3+}/\Sigma\text{Ti}$ values are almost identical to the recorded spectra and an example is shown in Fig. 7c.

EPR spectra of AD glasses are shown in Fig. 8a. Only Ti^{3+} , and not Ti^{4+} , contributes to an EPR spectrum and hence the spectral intensity should be directly related to the amount of Ti^{3+} . The spectra were parameterised using the difference in intensity between the maximum (3438 G) and minimum (3515 G) values. The variation in this intensity with the $f\text{O}_2$ determined from the modelling of the XANES results is shown in Fig. 8b and was fit, excluding the datum corresponding to the most reduced sample, to a modified version of Eq. (2). The $\log K^*$ obtained from this fit was 3.69(9), which is close to that determined from the XANES spectra (4.00). A similar result was obtained if the EPR spectra were parameterised using the area of the first peak. However, an almost equally good fit was obtained if $\log K^*$ was fixed at 4.00 and this fit is shown in Fig. 8b. Larger errors may be expected when quantifying $\text{Ti}^{3+}/\Sigma\text{Ti}$ from EPR spectra than XANES spectra because the EPR intensity depends on the number of Ti^{3+} cations, which will vary with any differences in the amount of sample in the analytical volume (for example, due to packing).

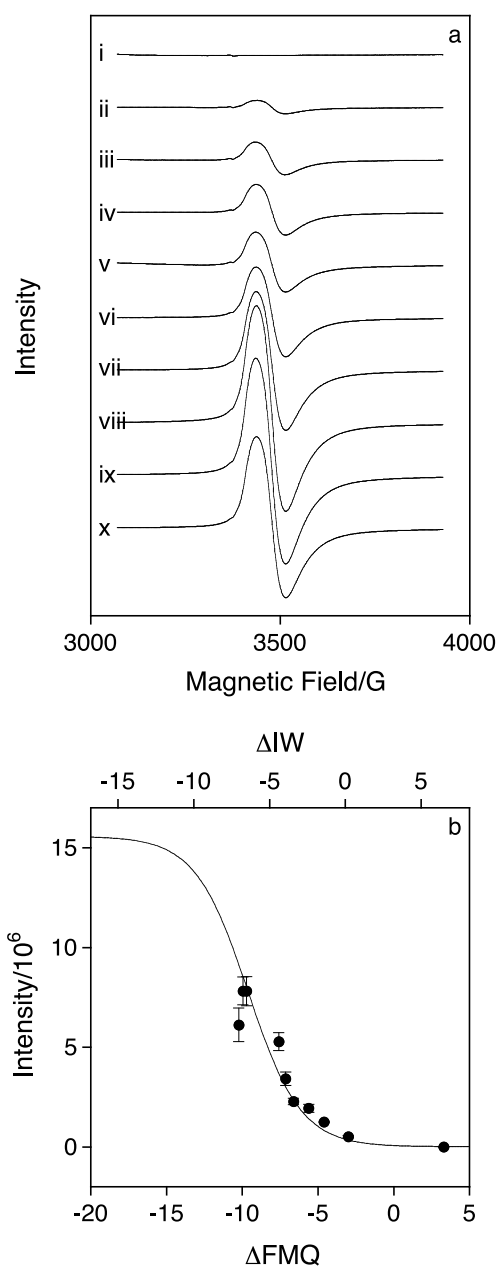


Fig. 8. (a) EPR spectra (first derivative of X-band absorption) of AD glasses containing 1 wt% TiO₂ quenched from melts equilibrated at 1400 °C and log*f*O₂s (determined from the model) relative to FMQ of (i) +3.3, (ii) −3.0, (iii) −4.6, (iv) −5.6, (v) −6.6, (vi) −7.1, (vii) −7.6, (viii) −9.7, (ix) −10.0, and (x) −10.2, and (b) the difference in intensity between the maximum (3438 G) and minimum (3515 G) values in the EPR spectrum as a function of ΔFMQ; the curve is the fit to the data (excluding the datum at ΔFMQ = −10.2) using a modified form of Eq. (2); uncertainties (one standard deviation) were determined from replicate spectra.

4. Discussion

Ti⁴⁺ is colourless while Ti³⁺ typically produces pink, purple or blue colours (e.g. Ihinger and Stolper, 1986). The development of an increasingly intense purple colour in these glasses, which contain no other redox variable elements, with decreasing *f*O₂ is indicative of increasing amounts of Ti³⁺. The EPR spectra also indicate increasing amounts of Ti³⁺ with decreasing *f*O₂ (Fig. 8a).

The spectra of all samples can be fit almost “perfectly” by a linear combination of the spectra of the most oxidised and reduced samples of the same composition. This indicates that the most reduced samples can

not contain any significant amounts of Ti²⁺, Ti⁰, or TiC (noting that the samples were prepared in graphite). log*f*O₂ was allowed to vary in the least squares regression model and for $-3.1 \leq \log fO_2 \leq -16.1$ the refined values are within ± 0.02 of the nominal values, which is smaller than the assumed uncertainty. In contrast, the calculated values of the samples prepared at nominally −18 and −20 are −16.35 and −16.62, respectively. A log*f*O₂ of −20 corresponds to a sample in equilibrium with graphite and 1 % CO and 99 % Ar (10 % CO and 90 % Ar for −18). While, in theory, the *f*O₂ should be buffered, the conditions are so extreme that a small ingress of atmospheric O₂ may exceed the buffering capacity of the system resulting in a higher *f*O₂ than expected. These conditions are more reduced than those under which SiO₂ oxygen sensors can operate and where the *f*O₂ can be calculated from the solubility of one of the small number of metals for which the required thermodynamic data is available (O’Neill and Eggins, 2002; Holzheid et al., 1997) and thus *f*O₂ can’t be determined independently. The correction of the nominal log*f*O₂ = −18 and −20 values means that the small differences between the spectra of the three most reduced samples are not because Ti³⁺/ΣTi was approaching 1 but because of the small differences in *f*O₂. This is illustrated in Fig. 4 where the correction in log*f*O₂ results in quite different sigmoidal fits and different values of log*K*′ (4.11(14) and 4.00(7) for the centroid and edge, respectively). The regression model finds that the most reduced samples of each composition have Ti³⁺/ΣTi between 0.54 and 0.67.

Ti³⁺/ΣTi is expected to be different for different compositions at the same *f*O₂. For other elements, log*K*′ has been shown to be linearly correlated with the optical basicity (Λ) of the composition (Cr, Berry et al., 2021a, 2021b; Sb, Miller et al., 2019; Eu, Burnham et al., 2015; Ce, Burnham and Berry, 2014). Optical basicity is a measure of the ability of O in a melt to donate electron density to a cation and hence stabilise positive charge (Duffy, 1993). Melt composition can be parameterised in other ways, such as NBO/T (non-bridging oxygens/tetrahedrally coordinated cations), but the correlations with log*K*′ are generally not as good (e.g. O’Neill and Berry, 2021). The relationship between log*K*′ and Λ found for Ti is shown in Fig. 9 and is given by:

$$\log K' = 1.90(19) + 3.44(32)\Lambda \quad (5)$$

The maximum difference between the predicted and determined values of log*K*′ is 0.02, which is taken as the uncertainty. This expression allows log*K*′ to be predicted for any melt or glass at 1400 °C since Λ can be easily calculated from the major element composition (Lebouteiller and Courtine, 1998; Duffy, 1989; see Supplementary Text). The correlation between log*K*′ and NBO/T is poor (R = 0.80).

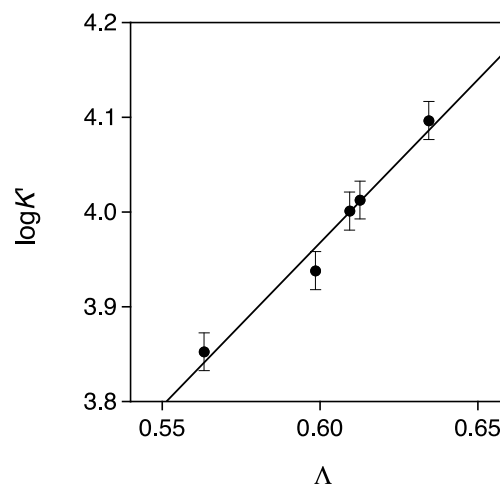


Fig. 9. Log*K*′ values at 1400 °C for the five compositions in Table 1 as a function of optical basicity (Λ). The line is the best fit to the data. The uncertainty in Λ is less than the size of the symbols.

A general expression for Ti^{3+}/Ti^{4+} can be obtained by recasting Eq. (1) in terms of ΔFMQ , where $\Delta FMQ = \log fO_2 - FMQ = \log fO_2 - (8.58 - 25050/T)$ (T in K; O'Neill et al., 2018). Thus at 1400 °C:

$$\log \frac{Ti^{3+}}{Ti^{4+}} = -\frac{1}{4} \Delta FMQ - 0.32(19) - 3.44(32)\Lambda \quad (6)$$

If the fO_2 dependence of $\log(Ti^{3+}/Ti^{4+})$ on temperature is parallel to FMQ, which is a reasonable assumption for Fe (Berry et al., 2018) and a good approximation for other elements (e.g. Cr, Berry et al., 2021a, 2021b; Eu, Burnham et al., 2015), then this equation can be used to relate Ti^{3+}/Ti^{4+} to ΔFMQ at any temperature. Under the same assumption:

$$\log K' = -1.84(19) + 3.44(32)\Lambda + 6262.5/T \quad (7)$$

The strong correlation between $\log K'$ and Λ means that Eq. (6) can be used to predict Ti^{3+}/Ti^{4+} in other compositions. Of particular interest are reduced extraterrestrial materials and average compositions of high-Ti Mare basalt, CV and CM chondrules, and Type A and B CAIs are given in Table 3. The relationship between $Ti^{3+}/\Sigma Ti$ and ΔFMQ (which is independent of temperature) for these compositions is shown in Fig. 10. The effect of composition is to change the fO_2 where $Ti^{3+} = Ti^{4+}$ by 1.5 log units, or at constant fO_2 to change $Ti^{3+}/\Sigma Ti$ from, for example, 0.5 in CM to 0.3 in Mare basalt. The effect of the difference in pressure between samples equilibrated at one atmosphere (the present study) and Solar condensates is likely to be negligible (cf. the effect of pressure on $Cr^{2+}/\Sigma Cr$; see Eq. (6) of Berry et al., 2021a, 2021b).

In this study, we chose to reference fO_2 to FMQ to facilitate comparison with studies of other redox variable elements (e.g. Berry et al., 2021a, 2021b; O'Neill et al., 2018). However, given the extremely reduced conditions required to produce Ti^{3+} in melts, and for comparison with the meteoritic literature, it is also convenient to reference fO_2 to IW. The $\log fO_2$ of the IW buffer is given by: $14.056 - 28776.5/T - 2.0384 \log T$ (evaluated from O'Neill and Pownceby, 1993) and its variation with temperature is almost parallel to that of FMQ. The difference between FMQ and IW can be calculated trivially with, for example, IW being more reduced by 3.3 log units at 1400 °C.

The Ti^{3+}/Ti^{4+} values predicted by the model of Borisov (2012) for the samples in the present study are compared to the experimentally determined values in Supplementary Fig. 3. The Borisov model significantly underestimates $Ti^{3+}/\Sigma Ti$ for four compositions (e.g. 0.14 compared to 0.58 for the most reduced sample of AD+Fo) but overestimates $Ti^{3+}/\Sigma Ti$ for the AD+Qz composition (0.80 compared to 0.67 for the most reduced sample). The fact that the predicted results for the AD+Qz composition differ so markedly from those of the other compositions suggests that the parameterisation of composition used by Borisov, which considers the mole fractions of SiO_2 and Al_2O_3 (and TiO_2 , which is insignificant in the present study) is not a good descriptor of how composition stabilises Ti^{3+} relative to Ti^{4+} . It is noteworthy that the mole fraction of SiO_2 in the AD+Qz composition is significantly different to that of our other four compositions. In contrast, the correlation between $\log K'$ and Λ in Fig. 9 suggests that Λ is an excellent descriptor.

The $\log K'$ values determined from literature data are given in Supplementary Table 3. The relationship between the $\log K'$ predicted using Eq. (7) and those determined experimentally is shown in Fig. 11. The

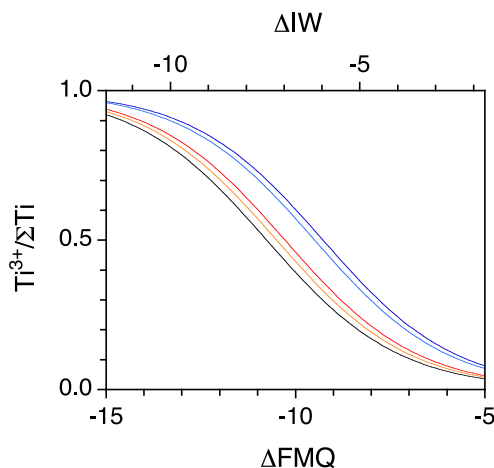


Fig. 10. Proportion of Ti as Ti^{3+} as a function of fO_2 , in log units relative to FMQ and IW, predicted using Eq. (6) for CV and CM (light and dark blue, respectively), CAI A and CAI B (orange and red, respectively), and Mare basalt (black).

agreement between the predicted and experimental values for the samples reported here, on which the model is based, is excellent, as expected. The temperature series data of Johnston (1965) are parallel to, but offset from, the 1:1 line. This indicates that the temperature dependence of Ti^{3+}/Ti^{4+} is (at least for this composition) close to

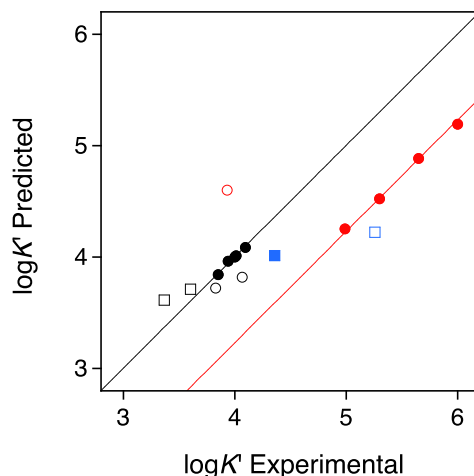


Fig. 11. Correlation between $\log K'$ predicted using Eq. (7) and determined experimentally in the present study (black circles; Table 1) and from literature data (Table S3) for FAD (open black circles) and FAS (open black squares) at 1500 and 1550 °C (Schreiber et al., 1978), ADA2 at 1250 °C (closed blue square; Schreiber et al., 1982), ADTi at 1300 °C (open red circle; Borisov et al. 2004), “slag” at 1500 °C (open blue square; Morizane et al., 1999), and $Na_2O.2SiO_2$ at 1000, 1085, 1200 and 1250 °C (closed red circles; Johnston, 1965). The lines are fits to the data from the present study and Johnston (1965) constrained to have a slope of 1.

Table 3

Compositions (wt%) of Type A and Type B CAIs (averages of values in Table 3 of Sylvester et al., 1993), CV and CM chondrules (median compositions; Table 2 of Hezel et al., 2018), and high-Ti Mare basalt (Table 1 of Danckwerth et al., 1979), the optical basicity (Λ) and NBO/T calculated for each composition, and $Ti^{3+}/\Sigma Ti$ calculated from the result of Eq. (6) at FMQ-5.3 (~IW-2) and FMQ-9.3 (~IW-6). Minor elements have been excluded.

Composition	SiO_2	Al_2O_3	MgO	CaO	TiO_2	Na_2O	FeO	Total	Λ	NBO/T	$Ti^{3+}/\Sigma Ti$ (IW-2)	$Ti^{3+}/\Sigma Ti$ (IW-6)
CAI A	24.23	34.07	5.25	33.90	1.41	0.33	0.70	99.89	0.674	0.763	0.046(29)	0.33(15)
CAI B	28.60	30.77	11.13	27.23	1.65	0.14	0.45	99.97	0.658	0.852	0.052(32)	0.36(15)
CV	45.22	3.55	35.48	2.76	0.17	0.40	–	87.58	0.601	2.186	0.080(46)	0.46(15)
CM	54.08	6.65	32.45	3.74	0.18	–	–	97.10	0.585	1.562	0.090(50)	0.50(15)
Mare basalt	38.0	8.3	10.4	10.2	12.6	0.4	19.0	98.9	0.693	1.321	0.040(26)	0.29(14)

parallel to FMQ (the slope of the correlation between $\log K'$ and $1/T$ is 6777(23)). The offset presumably arises from the optical basicity parameterisation being unable to account for differences in Ti^{3+} stability between such very different compositions. The model predicts the $\log K'$ s of the Schreiber et al. (1978) data within 0.25 (corresponding to a difference of less than one log unit in the $f\text{O}_2$ at which $\text{Ti}^{3+} = \text{Ti}^{4+}$), however, the differences are hard to explain given the broad similarities in composition. Not only does the temperature dependence of the Schreiber et al. (1978) data have a very different slope ($\sim 15000/T$) but the difference between the $\log K'$ of FAD and FAS is equal to that of the entire range found for the compositions studied here, for half the difference in optical basicity. It is possible, especially given the very small $\text{Ti}^{3+}/\Sigma\text{Ti}$ values of the Schreiber et al. (1978) samples (Fig. 1), that there was a background error in the Ti^{3+} determinations. The relative amounts of Ti^{3+} were determined by EPR spectroscopy, which was calibrated by redox titrations (which involve digesting a sample in acid, oxidising Ti^{3+} with Fe^{3+} , and then determining the amount of Fe^{2+} by titration with Ce^{4+}). The calibration curve relating Ti^{3+} determined by titration to EPR intensity is curved, whereas those shown for Cr and Eu are linear, as expected (Fig. 2 of Schreiber et al., 1978). As EPR intensity is directly proportional to Ti^{3+} it seems likely that the amount of Ti^{3+} may have been underestimated by titration (e.g. due to oxidation during digestion). The magnitude of the temperature dependence is also a significant difference between the model of Borisov (2012) and that presented here (33063/T compared to 6262.5/T). The coefficient of 33063 used by Borisov (2012) is much larger than that found for other elements (e.g. Kress and Carmichael, 1991; Burnham et al., 2015; Berry et al., 2021a, 2021b; Miller et al., 2023). Further, the value used for the Schreiber (1987) data in the Borisov model was 29500, which would decrease to ~ 15000 if $\log K'$ was evaluated using a fixed $\log f\text{O}_2$ coefficient of 0.25. It is thus not surprising that our model and that of Borisov (2012) do not agree. Accordingly, it is not surprising that our model does not predict the literature $\text{Ti}^{3+}/\Sigma\text{Ti}$ values from which the Borisov (2012) model was derived. It is difficult to speculate why these $\text{Ti}^{3+}/\Sigma\text{Ti}$ values are inconsistent with our model but we do note the difficulty of obtaining accurate values by redox titrations (see O'Neill et al., 2018) and that the composition of Borisov et al. (2004) contained over 25 wt% TiO_2 , for which concentrations a non-ideal dependence of $\text{Ti}^{3+}/\Sigma\text{Ti}$ on $f\text{O}_2$ is possible. A $\log K'$ of 3.91 at 1300 °C was determined from the partitioning of Ti as a function of $f\text{O}_2$ between various minerals and melts similar in composition to those studied here ($\log K' = K'_{\text{hom}}^{-1} = 1.24 \times 10^{-4}$; Table 7 Mallmann and O'Neill, 2009). The predicted value using Eq. (7) is 4.21, however, the experiments of Mallmann and O'Neill, 2009 used the same method to produce samples under extremely reduced conditions as in the present study (nominally $\log f\text{O}_2 = -18.6$ and -20.6 at 1300 °C), and their value of $\log K'$ strongly depends on the data for these samples. If the $\log f\text{O}_2$ s of these samples were less reduced than expected, as found here, then the $\log K'$ would increase (cf. Fig. 4) towards the predicted value. Finally, $\text{Ti}^{3+}/\Sigma\text{Ti}$ in synthetic Mare basalt glasses containing various Ti^{3+} -bearing minerals (e.g. pyroxene with $\text{Ti}^{3+}/\Sigma\text{Ti} = 0.25$) was found by Ti K-edge XANES spectroscopy to be 0 (± 0.05) at $\sim \text{IW}-2$ (Leitzke et al., 2018). Our model predicts $\text{Ti}^{3+}/\Sigma\text{Ti} = 0.040(26)$ for a Mare basalt at $\sim \text{IW}-2$ (Table 3), which is in agreement, within uncertainty.

There was no evidence for beam-induced changes in the oxidation state of Ti, however, any changes that went to completion in less than ~ 1 min would not have been detected. Such “fast” changes seem unlikely given that the dependence of $\text{Ti}^{3+}/\text{Ti}^{4+}$ on $f\text{O}_2$ can be described using the theoretical coefficient of 0.25 and that the resulting values of $\log K'$ correlate so well with composition.

5. Implications

At a given $f\text{O}_2$ the $\text{Ti}^{3+}/\Sigma\text{Ti}$ values reported here show a strong dependence on melt composition parameterised as optical basicity. This allows $\text{Ti}^{3+}/\Sigma\text{Ti}$ to be predicted for other geological compositions and,

at a given $f\text{O}_2$ and temperature, relative values of $\text{Ti}^{3+}/\Sigma\text{Ti}$ should be well constrained. The effect of temperature on $\text{Ti}^{3+}/\Sigma\text{Ti}$ is uncertain but it is probably a good approximation that the $f\text{O}_2$ at which $\text{Ti}^{3+} = \text{Ti}^{4+}$ has a temperature dependence parallel to that of FMQ (and hence also $\sim \text{IW}$), at least over the range of temperatures typical of basaltic and meteoritic melts. If this assumption is not correct and the change of $\text{Ti}^{3+}/\text{Ti}^{4+}$ with temperature was, for example, double that of the change in $f\text{O}_2$ of FMQ then a change in temperature from 1400 to 1600 °C would shift the point at which $\text{Ti}^{3+} = \text{Ti}^{4+}$ by ~ 1.5 log units to a higher value. Future work on determining the effect of temperature, by for example repeating the study reported here at different temperatures, would be useful to robustly define the predictive model for $\text{Ti}^{3+}/\text{Ti}^{4+}$.

Caution is required when trying to infer $f\text{O}_2$ from $\text{Ti}^{3+}/\text{Ti}^{4+}$ of natural glasses due to the possibility of electron exchange reactions between redox variable elements that may modify the expected oxidation state. For example, Cr^{2+} in a Fe^{3+} -bearing melt is not preserved on quenching to a glass due to the reaction $\text{Cr}^{2+} + \text{Fe}^{3+} = \text{Cr}^{3+} + \text{Fe}^{2+}$ (Berry et al., 2003). Similar reactions occur between Eu^{2+} and Fe^{3+} (Burnham et al., 2015), Ce^{4+} and Fe^{2+} (Burnham and Berry, 2014), and Cu^+ and Fe^{3+} (Miller et al., 2023). The likelihood of an exchange reaction involving two redox pairs can be inferred from the relative values of $\log K'$ (Schreiber, 1987), which correlate reasonably well with the standard reduction potentials of aqueous species. In natural melts the redox variable elements with an oxidation state of sufficient abundance under reduced conditions to potentially have an effect on $\text{Ti}^{3+}/\text{Ti}^{4+}$ are V, Cr, and Fe. The reaction $2\text{Ti}^{3+} + \text{Fe}^{2+} = 2\text{Ti}^{4+} + \text{Fe}^0$ has been postulated to explain the presence of metallic Fe in lunar basalts (e.g. Schreiber et al., 1982; Borisov, 2012). Differences in the oxidation state of V between synthetic glasses with different amounts of Ti have been used to infer that the reaction $\text{Ti}^{3+} + \text{V}^{4+} = \text{Ti}^{4+} + \text{V}^{3+}$ can completely remove Ti^{3+} (Sutton et al., 2005). This reaction was also invoked to explain differences in the oxidation state of V between synthetic analogues of high-Ti orange and low-Ti green lunar glasses (Sutton et al., 2005). Thus, $\text{Ti}^{3+}/\text{Ti}^{4+}$ in a lunar glass, or other reduced natural composition, may not correspond to that which was present in the melt or predicted by Eq. (6). In contrast, the Ti^{3+} and Ti^{4+} contents of minerals that crystallised from a melt should record $\text{Ti}^{3+}/\text{Ti}^{4+}$ of that melt. Hence, if $\text{Ti}^{3+}/\Sigma\text{Ti}$ can be determined for a mineral, and the partition coefficients of Ti^{3+} and Ti^{4+} are known, then $\text{Ti}^{3+}/\text{Ti}^{4+}$ of the original melt can be inferred and the $f\text{O}_2$ calculated from the bulk composition using Eq. (7). For an example of this approach using Cr and olivine see Bell et al. (2014).

Finally, the ability to predict $\text{Ti}^{3+}/\Sigma\text{Ti}$ of melts will help constrain models of mass-dependent Ti isotope fractionation (Leitzke et al., 2018). The oxidation state of Ti in a melt will determine its coordination environment and bond length, and hence the Ti-O force constant used to calculate isotopic fractionation (see Berry et al., 2021a, 2021b for Cr^{2+}).

Declaration of competing interest

The authors declare that they have no known competing financial interests or personal relationships that could have appeared to influence the work reported in this paper.

Acknowledgements

We thank John Spratt for assistance with the EPMA, Daniel Sells and the EPSRC UK National Electron Paramagnetic Resonance Facility at the University of Manchester for enabling us to acquire the EPR spectra, Diamond Light Source for the award of beamtime for proposal SP4516, and Hugh O'Neill for providing a template for the least squares minimisation model. A.J.B. thanks the Engineering and Physical Sciences Research Council (UK) for the award of a CNA studentship, which was used to support P.M.D. We thank Michael Ackerson and two anonymous reviewers for their comments on the work.

Appendix A. Supplementary material

Supplementary material includes (i) tables with $\log f_{\text{O}_2}$ values calculated from the Fe content of AD glasses quenched from melts equilibrated on Fe loops (Supplementary Table 1), energies of the pre-edge centroid and absorption edge at a normalised intensity of 0.8 determined from Ti K-edge XANES spectra (Supplementary Table 2), and $\log K'$ values for the oxidation of Ti^{3+} in silicate melts from the literature (Supplementary Table 3), (ii) figures showing the Ti K-edge XANES spectra of the AD+Fo, AD+Wo, AD+En, and AD+Qz glasses (Supplementary Fig. 1), the pre-edge region of the calculated AD spectrum with $\text{Ti}^{3+}/\Sigma\text{Ti} = 1$ (Supplementary Fig. 2), $\log(\text{Ti}^{3+}/\text{Ti}^{4+})$ values predicted by the model of Borisov (2012) and those determined experimentally (Supplementary Fig. 3), (iii) text explaining how to calculate optical basicity, and (iv) a spreadsheet containing the model for calculating $\text{Ti}^{3+}/\Sigma\text{Ti}$. Supplementary material to this article can be found online at <https://doi.org/10.1016/j.gca.2023.11.014>.

References

- Anderson, A.T., Bunch, T.E., Cameron, E.N., Haggerty, S.E., Boyd, F.R., Finger, L.W., James, O.B., Keil, K., Prinz, M., Ramdohr, P., El Goresy, A., 1970. Armalcolite: a new mineral from the Apollo 11 samples. Proc. Apollo 11 Lunar Sci. Conf., Geochim. Cosmochim. Acta, Sup. 1, 55–63.
- Beckett, J.R., Live, D., Tsay, F.-D., Grossman, L., Stolper, E., 1988. Ti^{3+} in meteoritic and synthetic hibonite. Geochim. Cosmochim. Acta 52, 1479–1495.
- Bell, A.S., Burger, P.V., Le, L., Shearer, C.K., Papike, J.J., Sutton, S.R., Newville, M., Jones, J., 2014. XANES measurements of Cr valence in olivine and their applications to planetary basalts. Am. Mineral. 99, 1404–1412.
- Berry, A.J., Shelley, J.M.G., Foran, G.J., O'Neill, H.St.C., Scott, D.R., 2003. A furnace design for XANES spectroscopy of silicate melts under controlled oxygen fugacities and temperatures to 1773 K. J. Synch. Rad. 10, 332–336.
- Berry, A.J., O'Neill, H.St.C., Scott, D.R., Foran, G.J., Shelley, J.M.G., 2006. The effect of composition on $\text{Cr}^{2+}/\text{Cr}^{3+}$ in silicate melts. Am. Mineral. 91, 1901–1908.
- Berry, A.J., Walker, A.M., Hermann, J., O'Neill, H.St.C., Foran, G.J., Gale, J.D., 2007. Titanium substitution mechanisms in forsterite. Chem. Geol. 242, 176–186.
- Berry, A.J., Schofield, P.F., Kravtsova, A.N., Miller, L.A., Stephen, N.R., Walker, A.M., Soldatov, A.V., Ireland, T.R., Geraki, K., Mosselmans, J.F.W., 2017. The limitations of hibonite as a single-mineral oxybarometer for early solar system processes. Chem. Geol. 466, 32–40.
- Berry, A.J., Stewart, G.A., O'Neill, H.St.C., Mallmann, G., Mosselmans, J.F.W., 2018. A re-assessment of the oxidation state of iron in MORB glasses. Earth Planet. Sci. Lett. 482, 114–123.
- Berry, A.J., O'Neill, H.St.C., 2004. A XANES determination of the oxidation state of chromium in silicate glasses. Am. Mineral. 89, 790–798.
- Berry, A.J., O'Neill, H.St.C., Foran, G.J., 2021a. The effect of temperature and pressure on the oxidation state of chromium in silicate melts. Contrib. Mineral. Petrol. 176, 40.
- Berry, A.J., Miller, L.A., O'Neill, H.St.C., Foran, G.J., 2021b. The coordination of Cr^{2+} in silicate glasses and implications for mineral-melt fractionation of Cr isotopes. Chem. Geol. 586, 120483.
- Borisov, A.A., 2012. The $\text{Ti}^{4+}/\text{Ti}^{3+}$ Ratio of magmatic melts: Application to the problem of the reduction of lunar basalts. Petrology 20, 391–398.
- Burnham, A.D., Berry, A.J., 2014. The effect of oxygen fugacity, melt composition, temperature and pressure on the oxidation state of cerium in silicate melts. Chem. Geol. 366, 52–60.
- Burnham, A.D., Berry, A.J., Halse, H.R., Schofield, P.F., Cibir, G., Mosselmans, J.F.W., 2015. The oxidation state of europium in silicate melts as a function of oxygen fugacity, composition and temperature. Chem. Geol. 411, 248–259.
- Burns, R.G., Huggins, F.E., 1973. Visible-region absorption spectra of a Ti^{3+} fassaite from the Allende meteorite: a discussion. Am. Mineral. 58, 955–961.
- Chase, M.W., 1998. NIST-JANAF Thermochemical Tables, fourth ed. J. Phys. Chem. Ref. Data Monograph 9.
- Danckwirth, P.A., Hess, P.C., Rutherford, M.J., 1979. The solubility of sulfur in high- TiO_2 mare basalts. Proc. Lunar Planet. Sci. Conf. 10, 517–530.
- Dowty, E., Clark, J.R., 1973. Crystal structure refinement and optical properties of a Ti^{3+} fassaite from the Allende meteorite. Am. Mineral. 58, 230–242.
- Doyle, P.M., Schofield, P.F., Berry, A.J., Walker, A.M., Knight, K.S., 2014. Substitution of Ti^{3+} and Ti^{4+} in hibonite (CaAl_2O_7). Am. Mineral. 99, 1369–1382.
- Doyle, P.M., Berry, A.J., Schofield, P.F., Mosselmans, J.F.W., 2016. The effect of site geometry, Ti content and Ti oxidation state on the Ti K-edge XANES spectrum of synthetic hibonite. Geochim. Cosmochim. Acta 187, 294–310.
- Duffy, J.A., 1989. Optical basicity of titanium(IV) oxide and zirconium(IV) oxide. J. Am. Ceramic Soc. 72, 2012–2013.
- Duffy, J.A., 1993. A review of optical basicity and its applications to oxidic systems. Geochim. Cosmochim. Acta 57, 3961–3970.
- Farges, F., Brown, Jr, G.E., Rehr, J.J., 1996. Coordination chemistry of Ti(IV) in silicate glasses and melts: I. XAFS study of titanium coordination in oxide model compounds. Geochim. Cosmochim. Acta 60, 3023–3038.
- Farges, F., Brown, Jr, G.E., 1997. Coordination chemistry of titanium(IV) in silicate glasses and melts: IV. XANES studies of synthetic and natural volcanic glasses and tektites at ambient temperature and pressure. Geochim. Cosmochim. Acta 61, 1863–1870.
- Friel, J.F., Harker, R.I., Ulmer, G.C., 1977. Armalcolite stability as a function of pressure and oxygen fugacity. Geochim. Cosmochim. Acta 41, 403–410.
- Harris, C.R., Millman, K.J., van der Walt, S.J., Gommers, R., Virtanen, P., et al., 2020. Array programming with NumPy. Nature 585, 357–362.
- Hezel, D.C., Harak, M., Libourel, G., 2018. What we know about elemental bulk chondrule and matrix compositions: Presenting the ChondriteDB Database. Chem. Erde 78, 1–14.
- Holzheid, A., Palme, H., Chakraborty, S., 1997. The activities of NiO, CoO and FeO in silicate melts. Chem. Geol. 139, 21–38.
- Ihinger, P.D., Stolper, E., 1986. The color of meteoritic hibonite: an indicator of oxygen fugacity. Earth Planet. Sci. Lett. 78, 67–79.
- Jayasuriya, K.D., O'Neill, H.St.C., Berry, A.J., Campbell, S.J., 2004. A Mössbauer study of the oxidation state of iron in silicate melts. Am. Mineral. 89, 1597–1609.
- Johnston, W.D., 1965. Oxidation-reduction equilibria in molten $\text{Na}_2\text{O} \cdot 2\text{SiO}_2$ glass. J. Am. Ceramic Soc. 48, 184–190.
- Jurewicz, S.R., Jones, J.H., Fegley Jr, B., 1995. Experimental partitioning of Zr, Nb, and Ti between platinum group metals and silicate liquid: implications for the origin of refractory metal nuggets in carbonaceous chondrites. Earth Planet. Sci. Lett. 132, 183–198.
- Krause, M.O., Oliver, J.H., 1979. Natural widths of atomic K and L levels, K α X-ray lines and several KLL Auger lines. J. Phys. Chem. Ref. Data 8, 329–338.
- Kress, V.C., Carmichael, I.S.E., 1991. The compressibility of silicate liquids containing Fe_2O_3 and the effect of composition, temperature, oxygen fugacity and pressure on their redox states. Contrib. Mineral. Petrol. 108, 82–92.
- Lebouteiller, A., Courtine, P., 1998. Improvement of a bulk optical basicity table for oxidic systems. J. Solid State Chem. 137, 94–103.
- Leitzke, F.P., Fonseca, R.O.C., Göttlicher, J., Steingner, R., Jahn, S., Prescher, C., Lagos, M., 2018. Ti K-edge XANES study on the coordination number and oxidation state of titanium in pyroxene, olivine, armalcolite, ilmenite, and silicate glass during mare basalt petrogenesis. Contrib. Mineral. Petrol. 173, 103.
- Miller, L.A., Berry, A.J., O'Neill, H.St.C., Wykes, J., Newville, M., Lanzirotti, T., 2023. The effect of composition, temperature and pressure on the oxidation state and coordination environment of copper in silicate melts. Geochim. Cosmochim. Acta 364, 129–147.
- Mallmann, G., O'Neill, H.St.C., 2009. The crystal/melt partitioning of V during mantle melting as a function of oxygen fugacity compared with some other elements (Al, P, Ca, Sc, Ti, Cr, Fe, Ga, Y, Zr and Nb). J. Petrology 50, 1765–1794.
- Miller, L.A., O'Neill, H.St.C., Berry, A.J., Glover, C.J., 2019. The oxidation state and coordination environment of antimony in silicate glasses. Chem. Geol. 524, 283–294.
- Morizane, Y., Ozturk, B., Fruehan, R.J., 1999. Thermodynamics of TiO_2 in blast furnace-type slags. Metal. Material. Trans. 30B, 29–43.
- Mosselmans, J.F., Quinn, P.D., Dent, A.J., Cavill, S.A., Moreno, S.D., Peach, A., Leicester, P.J., Keylock, S.J., Gregory, S.R., Atkinson, K.D., Rosell, J.R., 2009. I18 - the microfocus spectroscopy beamline at the Diamond Light Source. J. Synch. Rad. 16, 818–824.
- O'Neill, H.St.C., Berry, A.J., Mallmann, G., 2018. The oxidation state of iron in Mid-Ocean Ridge Basaltic (MORB) glasses: Implications for their petrogenesis and oxygen fugacities. Earth Planet. Sci. Lett. 504, 152–162.
- O'Neill, H.St.C., Eggins, S.M., 2002. The effect of melt composition on trace element partitioning: an experimental investigation of the activity coefficients of FeO, NiO, CoO, MoO₂ and MoO₃ in silicate melts. Chem. Geol. 186, 151–181.
- O'Neill, H.St.C., Berry, A.J., 2006. Activity coefficients at low dilution of CrO, NiO and CoO in melts in the system CaO-MgO-Al₂O₃-SiO₂ at 1400 °C: using the thermodynamic behaviour of transition metal oxides in silicate melts to probe their structure. Chem. Geol. 231, 77–89.
- O'Neill, H.St.C., Berry, A.J., 2021. The oxidation state of chromium in basaltic silicate melts. Geochim. Cosmochim. Acta. 306, 304–320.
- O'Neill, H.St.C., Pownceby, M.I., 1993. Thermodynamic data from redox reactions at high temperatures. I. An experimental and theoretical assessment of the electrochemical method using stabilized zirconia electrolytes, with revised values for the Fe-FeO, Co-CoO, Ni-NiO and Cu-Cu₂O oxygen buffers, and new data for the W-WO₂ buffer. Contrib. Mineral. Petrol. 114, 296–314.
- Papike, J.J., Karner, J.M., Shearer, C.K., 2005. Comparative planetary mineralogy: valence state partitioning of Cr, Fe, Ti, and V among crystallographic sites in olivine, pyroxene, and spinel from planetary basalts. Am. Mineral. 90, 277–290.
- Ravel, B., Newville, M., 2005. ATHENA, ARTEMIS, HEPHAESTUS: data analysis for X-ray absorption spectroscopy using IFEFFIT. J. Synch. Rad. 12, 537–541.
- Schreiber, H.D., 1987. An electrochemical series of redox couples in silicate melts: a review and applications to geochemistry. J. Geophys. Res. 92, 9225–9232.
- Schreiber, H.D., Thanyasiri, T., Lach, J.J., Legere, R.A., 1978. Redox equilibria of Ti, Cr, and Eu in silicate melts: reduction potentials and mutual interactions. Phys. Chem. Glass. 19, 126–139.
- Schreiber, H.D., Balazs, G.B., Shaffer, A.P., Jamison, P.L., 1982. Iron metal production in silicate melts through the direct reduction of Fe(II) by Ti(III), Cr(II), and Eu(II). Geochim. Cosmochim. Acta 46, 1891–1901.
- Simon, S.B., Sutton, S.R., Grossman, L., 2007. Valence of titanium and vanadium in pyroxene in refractory inclusion interiors and rims. Geochim. Cosmochim. Acta 71, 3098–3118.
- Simon, S.B., Sutton, S.R., 2017. Valence of Ti, V, and Cr in Apollo 14 aluminous basalts 14053 and 14072. Meteoritics Planet. Sci. 52, 2051–2066.

- Sutton, S.R., Jones, K.W., Gordon, B., Rivers, M.L., Smith, J.V., 1993. Reduced chromium in olivine grains from lunar basalt 15555: X-ray absorption near edge structure (XANES). *Geochim. Cosmochim. Acta* 57, 461–468.
- Sutton, S.R., Karner, J.M., Delaney, J.S., Papike, J.J., Shearer, C.K., Newville, M., Rivers, M., Eng, P., Dyar, M.D., 2005. Vanadium K edge XANES of synthetic and natural basaltic glasses and application to microscale oxygen barometry. *Geochim. Cosmochim. Acta* 69, 2333–2348.
- Sutton, S.R., Goodrich, C.A., Wirick, S., 2017. Titanium, vanadium and chromium valences in silicates of ungrouped achondrite NWA 7325 and ureilite Y-791538 record highly-reduced origins. *Geochim. Cosmochim. Acta* 204, 313–330.
- Sylvester, P.J., Simon, S.B., Grossman, L., 1993. Refractory inclusions from the Leoville, Efremovka, and Vigarano C3V chondrites: Major element differences between Types A and B, and extraordinary refractory siderophile element compositions. *Geochim. Cosmochim. Acta* 57, 3763–3784.
- Tranell, G., Ostrovski, O., Jahanshahi, S., 2002. The equilibrium partitioning of titanium between Ti^{3+} and Ti^{4+} valency states in CaO-SiO₂-TiO_x slags. *Metallurg. Mat. Trans. B* 33, 61–67.
- Waychunas, G.A., 1987. Synchrotron radiation XANES spectroscopy of Ti in minerals: effects of Ti bonding distances, Ti valence, and site geometry on absorption edge structure. *Am. Mineral.* 72, 89–101.